




Relationship Between the Static and Dynamic Bulk Moduli of Argillites

O. O. BLAKE,¹  R. RAMSOOK,¹ D. R. FAULKNER,² and U. C. IYARE¹

Abstract—Bulk modulus is one of the mechanical properties used in any rock engineering related project. This property can be measured statically, where it is derived from stress–strain data, and dynamically, where it is derived from P- and S-wave velocities. The static bulk modulus is generally different from the corresponding dynamic bulk modulus. As the static bulk modulus is required in computation or modelling of the deformation of the rock when it is stressed hydrostatically, empirical relationships between the static and dynamic bulk moduli are needed to convert the dynamic bulk modulus to static values. In this study, the static and dynamic bulk moduli were measured simultaneously, at effective pressures up to 130 MPa, for dry and fluid-saturated argillites. The samples were collected from four different lithofacies within the upper Naparima Hill Formation, Trinidad. The results show that the dynamic bulk modulus is greater than the static bulk modulus, except for hard lithofacies under dry conditions where the static and dynamic moduli are approximately equal. Under saturated conditions, the porosity plays a key role in increasing the difference between the static and dynamic bulk moduli. A linear relationship with high correlation (R^2 greater than 0.85) was established between the static and dynamic bulk moduli, which is dependent on the effective pressure and saturation state.

Keywords: Bulk modulus, Elastic properties, Mudstone, Argillite, Naparima hill formation.

List of Symbols

K_{static}	Static bulk modulus
$K_{dynamic}$	Dynamic bulk modulus
K_f	Bulk modulus of the pore fluid
K_{fr}	Bulk modulus of the rock frame
V_p	P-wave velocity
V_s	S-wave velocity
L	Length of the specimen
T	Travel time of the waves
ρ	Density of the specimen

1. Introduction

Elastic properties of rocks and their pressure and saturation dependence are of interest in many areas including reservoir geomechanics; civil, mining and petroleum engineering; fault zone characterization; etc. Elastic properties include elastic parameters such as Poisson's ratio, Young's modulus, bulk modulus, and shear modulus. Each parameter describes the elastic deformation of a rock in a different manner. The elastic properties can be calculated statically, where stress is applied to deform the rock slowly and the resultant strain is measured. They can also be determined by inverting P- and S-wave velocities measurements, referred to as the dynamic properties. However, the two types of elastic properties are different. The difference between the static and dynamic elastic properties are caused by factors such as the presence of microfractures, stress induced anisotropy, the magnitude of the strain amplitude applied, the frequency at which the moduli is determined, the saturation state, and the type of pore fluid (Adam & Batzle, 2008; Adelinet et al. 2010; Batzle et al. 2001, 2006; Blake & Faulkner, 2016; Hammond et al. 1979; Jizba, 1991; Müller et al. 2010; Tutuncu et al. 1998a, b).

The static elastic properties are required in computing or modelling the deformation of rock when it is stressed. Hence, relationships need to be established to convert the dynamic elastic properties to static ones. Here, we will focus on the relationship between static and dynamic bulk moduli. The bulk modulus generally describes the resistance of the rock to hydrostatic compression. The inverse of bulk modulus gives the compressibility. Simmons and Brace (1965) found that the static to dynamic bulk modulus ratio ($K_{static}/K_{dynamic}$) of granites, quartzite and limestone is approximately 0.5 at atmospheric

¹ Petroleum Geoscience, Department of Chemical Engineering, University of the West Indies, St. Augustine, Trinidad and Tobago. E-mail: oshaine.blake@sta.uwi.edu

² Department of Earth, Ocean and Ecological Sciences, University of Liverpool, Liverpool, UK.

pressure and close to 1 at confining pressures of 300 MPa and above. Cheng and Johnston (1981) found that $K_{static}/K_{dynamic}$ of dry oil shale samples is approximately 0.7 and remains fairly constant up to confining pressures of 200 MPa. Jizba and Nur (1990) found a linear relationship between the static and dynamic bulk moduli (K_{static} and $K_{dynamic}$) for dry tight gas sandstones sample:

$$K_{static} = 1.293K_{dynamic} - 11.634 \quad (1)$$

Bakhorji and Schmitt (2010) found a consistent trend of the static to dynamic ratio of dry and water saturated carbonate samples to approximately 0.5. Adelinet et al. (2010) found a systematic small difference between static and dynamic bulk moduli of dry Basalt samples pressurized up to 200 MPa. Yan et al. (2017) found that the dynamic bulk modulus is approximately equal to the static bulk modulus when the pore stiffness of dry and water saturated sandstone is greater than 6 GPa.

The relationship that relates dynamic to static bulk modulus for argillites is non-existent in the literature. Argillites are indurated mudstones that have relatively high strength and low permeability. These rocks are often used in civil engineering projects, are unconventional petroleum reservoirs granted that the organic content is high, and serve as waste repository. In this study, the static and dynamic bulk moduli of Naparima Hill Formation argillites were measured simultaneously under both wet (fully water saturated) and dry (atmospheric) conditions as a function of effective pressure (confining pressure minus pore pressure) up to 130 MPa. The aim of this work is to determine if a relationship exists between the static and dynamic bulk moduli for argillites. If a relationship does exist, we want to explore if it is dependent on saturation state and effective pressure (equivalent to burial depth).

2. Methodology

2.1. Sample Description and Preparation

Experiments were carried out on rock samples that were retrieved from seven different outcrop locations (referred to as NHS1, NHS3, NHS4, NHS7,

NHS10, NHS13 and NHS14) of the Naparima Hill Formation, Trinidad (Fig. 1). The lithology of the Naparima Hill Formation has been described as organic-rich argillites (Pindell & Kennan, 2009) and the lithofacies considered similar to the siliceous argillites found within the Monterey Formation in California, USA. The porosity and permeability of these argillites ranged from 6 to 31% and 10^{-20} to 10^{-18} m², respectively (Iyare et al. 2020). Petrographic investigation conducted by Iyare et al. (2020) on the studied outcrop samples showed that the samples are primarily quartz, with calcite present as a secondary mineral and cement. Clay minerals (e.g. illite and kaolinite) are also present, but are in small quantity (Fig. 2a). The thin section analysis of the outcrop samples revealed four lithofacies associations: Lithofacies *a* (location NHS7) is mainly an oil stained, siliceous calcareous mudstone (Fig. 2b); Lithofacies *b* (locations NHS1, NHS3, NHS4 and NHS14) is mainly a calcite cemented, calcareous mudstone interbedded with black chert (Fig. 2c–f); Lithofacies *c* (location NHS13) is mainly an oil-filled, carbonate rich mudstone with nodular chert (Fig. 2g) and Lithofacies *d* (location NHS10) is mainly a poorly sorted, siliceous mudstone (Fig. 2h).

A significant amount of the outcrop surface was removed from each location to retrieve fresh in-situ block samples. The outcrops are resistant to weathering due to their dense textures and high silica content (Fig. 2). Cylindrical specimens of 20 mm diameter were cored perpendicular to the bedding of the outcrops (see Fig. 3 for specimen preparation). The lengths of the specimens were between 50 and 55 mm and the ends were squared (± 0.02 mm) in accordance with ASTM D7012 (2014) and ASTM D4543 (2019) suggested methods. The oil within the specimens was then removed using toluene in the soxhlet extractor method, which increases the porosity and surface area (Gupta et al. 2017). Strain gauges (axial and radial) were attached to the centre of the specimens and then the specimens were placed in PVC jacket. The electrical connections of the strain gauges were fed out through small holes in the jacket, which were then sealed by an epoxy adhesive.

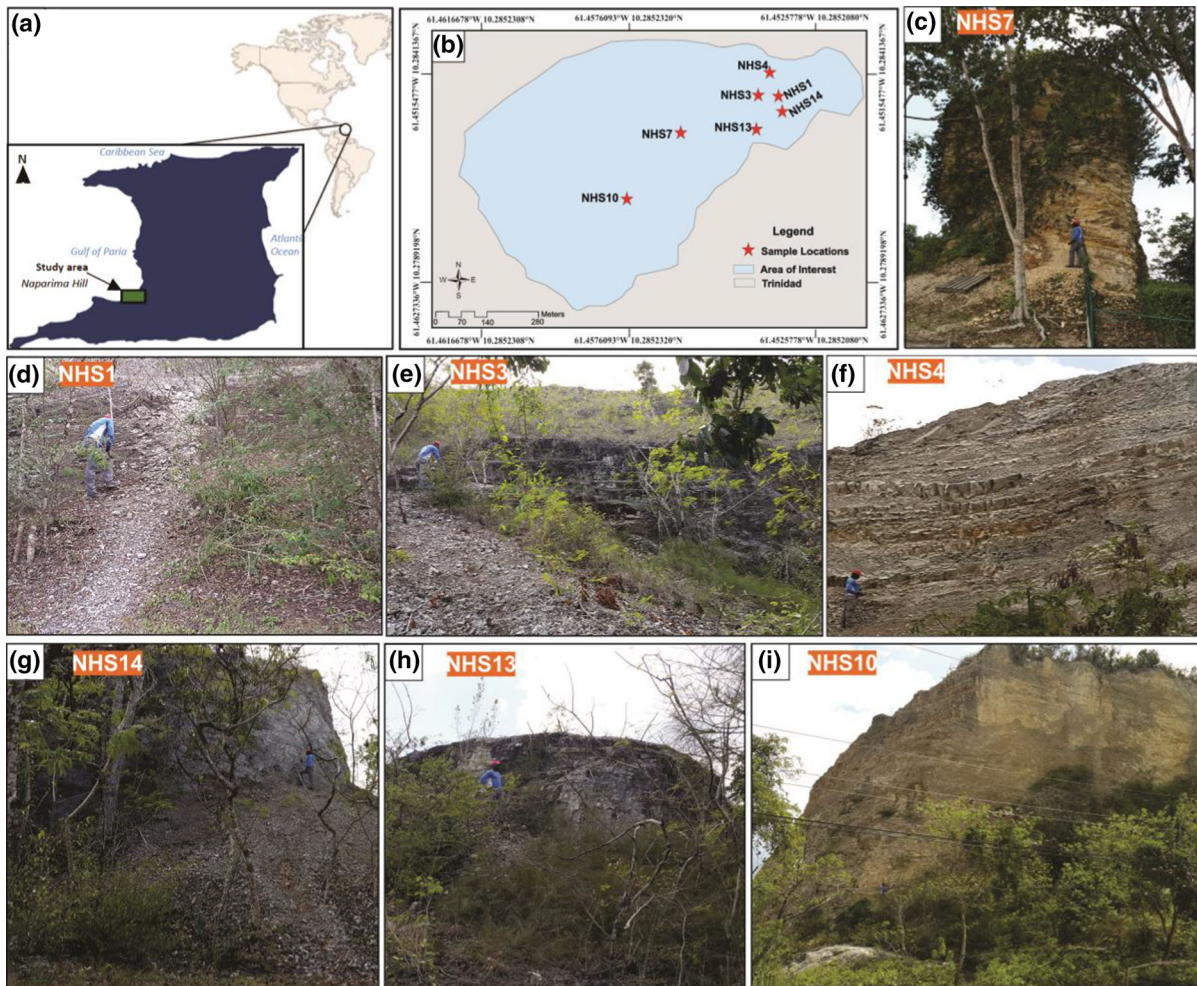


Figure 1

The study area (a). (b) provides a zoom-in on the study area. (c–i) show the locations of where the Naparima Hill Formation outcrop was sampled

2.2. Experimental Procedure

Static and dynamic measurements were conducted using a servo-controlled triaxial apparatus that is installed at the Geomechanics Laboratory, University of West Indies (Fig. 4). Blake and Faulkner (2016) provided more details on the apparatus. The apparatus has the capability to measure P- and S-wave velocities at 1.5 MHz under confining and pore pressures as high as 200 MPa. Experiments were carried out on dry and saturated specimens at effective pressures (confining pressure minus pore pressure) up to 130 MPa. To ensure that the specimens were completely dried, they were placed in an

oven at 50 °C for seven days. For saturated tests, the specimens were placed in a bath of de-ionized water under vacuum. The specimens are then removed from the water bath and placed in the triaxial apparatus where de-ionized water was pumped, at a pressure of 10 MPa, into the specimens from both ends of the specimen, using the upstream and downstream pore pressure connections. The pore pressure controller was used to apply this constant pressure and to ensure that the pressure was equilibrated within the specimen pressure, which took hours to achieve due to the low permeability of the specimens. Confining pressure was applied to the specimens using the confining

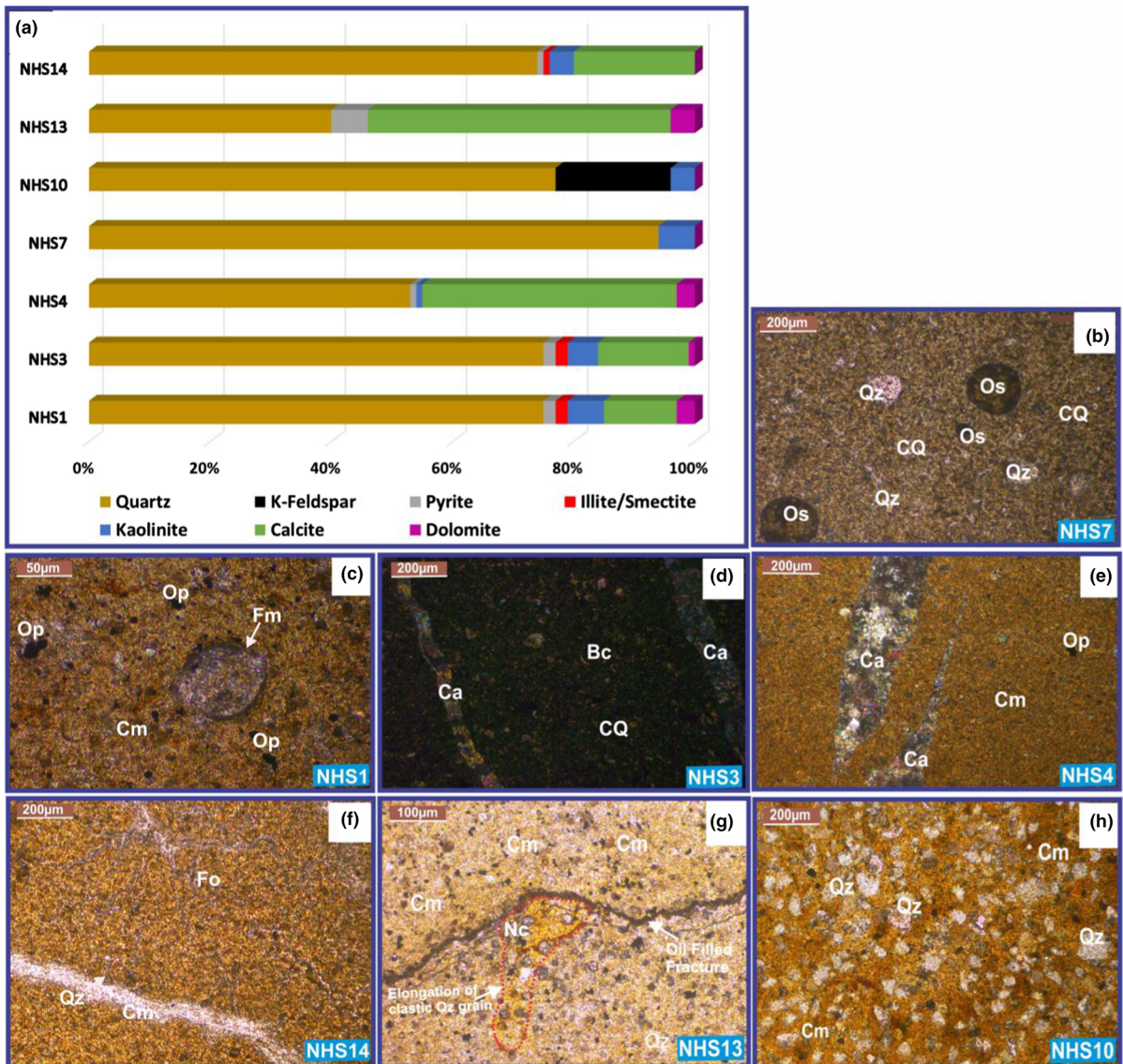


Figure 2

X-ray diffraction (XRD) (a) and Photomicrographs (b–h) of the studied outcrop locations within the Naparima Hill Formation (modified from Iyare et al. 2020). Note: (Qz) Quartz; (Cm) Chert matrix, (Op) Oil particle; (Os) Oil stain; (Ca) Calcite filled fracture; (CQ) Calcite-Quartz matrix; (Nc) Nodular chert (Fo) Oil filled fracture; (Fm) Foraminifera; (Bc) Bioclasts

pressure pump and controller (Fig. 4b). The PVC jacket in which the specimens were placed, separated the confining fluid from the pore fluid.

The axial and radial strain gauges that were attached to the specimens were used to monitor the deformation within the specimens when they were subjected to increasing effective pressures. The strain gauges were connected in a Wheatstone bridge

configuration using a strain gauge amplifier. The output of the axial and radial strain gauges are identical, and were used to determine the static bulk properties. The static bulk modulus was determined by differentiating the volumetric strain (axial or radial strain multiplied by 3) vs effective pressure curve at 10, 30, 50, 70, 90, 110 and 130 MPa

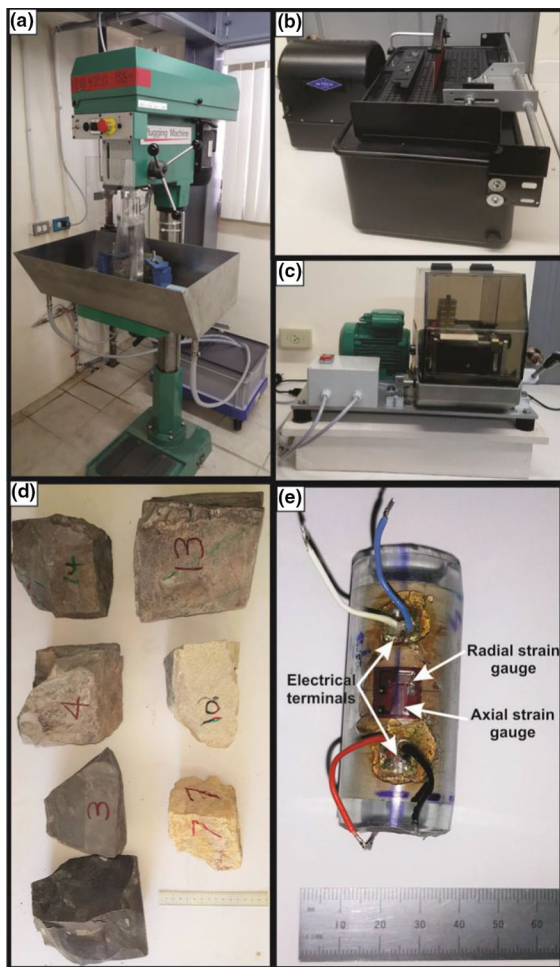


Figure 3

Preparation of sample. **a** Plugging machine to extract 20 mm diameter plugs. **b** Saw to trim the ends of the plug to the required length (50–55 mm). **c** Precision-end grinder to square ends of plugs to ± 0.02 mm. **d** Intact samples from the seven outcrop locations. **e** Typical prepared sample (sample from NHS10 is shown in this example) placed inside PVC jacket. Electrical wires are attached to the terminals of the axial and radial strain gauges and fed through hole in jacket. The hole is then sealed with a compliant epoxy resin

effective pressure (Cheng & Johnston, 1981) (Fig. 5a).

Dynamic elastic properties were calculated by the inversion of P- and S-wave velocities. P- and S-wave piezoelectric ceramics (PZT-5A) placed in the top and bottom loading platens (Fig. 4c) were used to generate P- or S-wave at one end of the specimen and received the P- or S-wave at the other end. Backing material made from sintered stainless steel of 0.5 μm pore size and 0.125 inch thick was placed on the

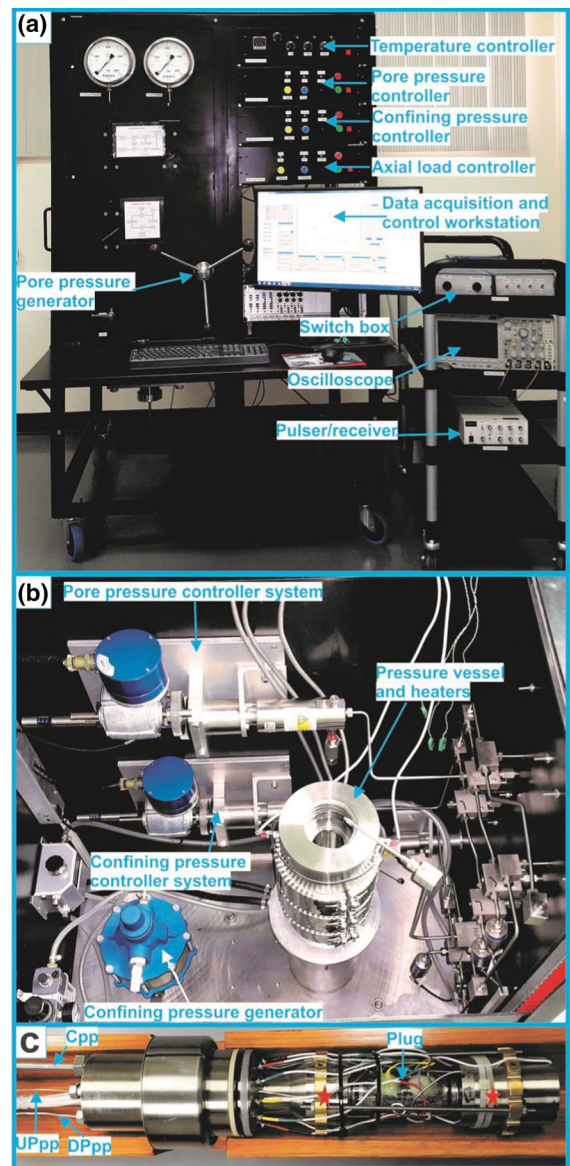


Figure 4

Triaxial apparatus. **a** Front view showing pore pressure generator, controllers, and ultrasonic system (switchbox, oscilloscope and pulser/receiver). **b** Inside view showing confining and pore pressure controller systems, confining pressure generator, and pressure vessel with heaters. **c** Seismic sample showing confining pressure pipe (Cpp), upstream pore pressure pipe (Uppp), downstream pore pressure pipe (Dppp), plugged cylindrical sample, strain gauge and P- and S-wave piezoceramic connecting wires. The red stars indicate the locations of where the P- and S-wave piezoceramic ceramics are housed. The seismic sample assembly is placed inside the pressure vessel

piezoelectric ceramics. A pulser/receiver (JSR DPR300 Pulser/Receiver) was used for the excitation

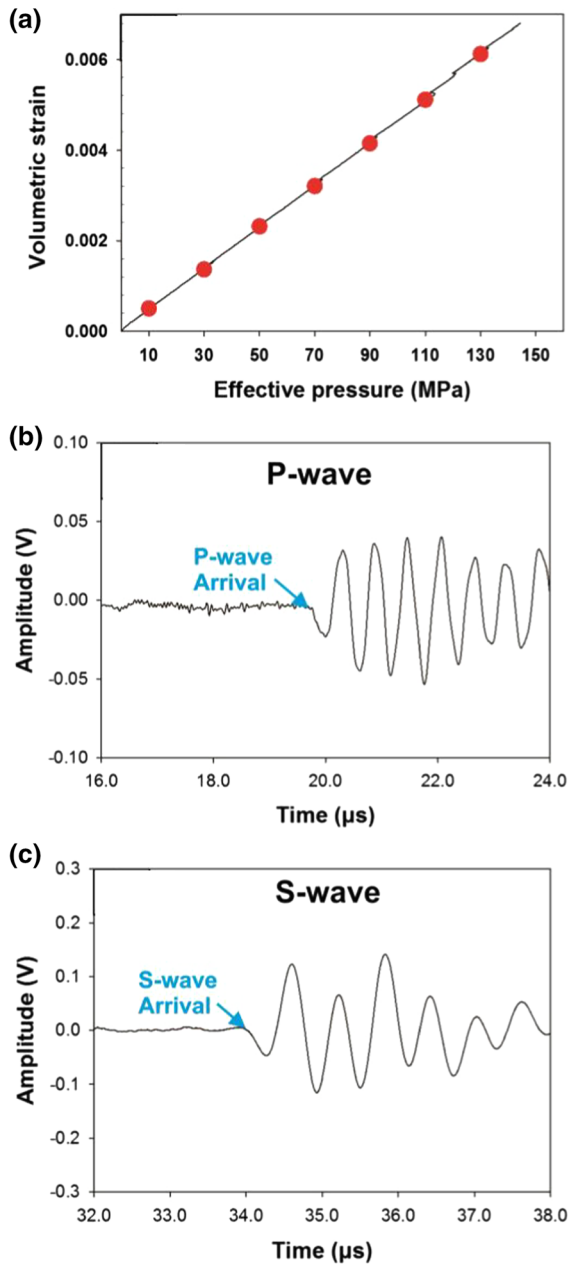


Figure 5

Example of strain data as a function of effective pressure (a), and P- and S-wave arrivals at 10 MPa effective pressure (b, c) from location NHS4 (lithofacies *b*), under dry conditions. The red circles on the volumetric strain curve indicate the effective pressure at which P- and S-wave data were recorded. The P-wave arrived at 19.71 μs and the S-wave arrived at 34.02 μs

and amplification of the received signals. A digital oscilloscope with high time-based accuracy (Tektronix MDO3034) was employed to display and

record the amplified ultrasonic waves. For accurate and reliable P- and S-wave measurements, ASTM D2845-08 (2008) was adhered to, which significantly reduced the P to S-waves and S- to P-waves converted waves that usually obscure the S-wave arrival. The P- and S-wave arrivals are very clear and can be easily picked (Fig. 5b, c). The effective pressure was held constant for ~ 10 s at 10, 30, 50, 70, 90, 110 and 130 MPa, to record the velocity data. P- and S- wave velocities were calculated by dividing the specimen's length (L) by the P- and S-waves travel time (t):

$$V_p \text{ or } V_s = L/t \quad (2)$$

where V_p is the P-wave velocity and V_s is the S-wave velocity. The specimen length changes with increasing effective pressure, which is determined by the axial strain gauge. The corrected specimen length is used in the velocity calculations. By assuming the specimens are isotropic, the dynamic bulk modulus, $K_{dynamic}$, can be estimated from the P- and S-wave velocities using the well-known relationships for isotropic materials (e.g. Cheng & Johnston, 1981):

$$K_{dynamic} = \rho \left(V_p^2 - \frac{4}{3} V_s^2 \right) \quad (3)$$

where ρ is the density of the specimen. A detailed analysis of isotropy assumption is presented in the "Discussion" section. The change in the specimen's density, calculated from the static volumetric strain data and porosity data from Iyare et al. (2020), was accounted for in the calculations.

3. Results

Figure 6 shows P- and S- wave velocities and density as a function of effective pressure for both dry and saturated conditions from which dynamic bulk moduli are calculated. The P- and S-wave velocities and density increase slightly with increasing effective pressure. Specimens from locations NHS7 and NHS10, (soft rocks from lithofacies *a* and *d*) experience a greater rate of velocity increase. Saturation of the specimens causes the P- and S-wave velocities to decrease, with the exception of the specimen from NHS7, where the P-wave velocity

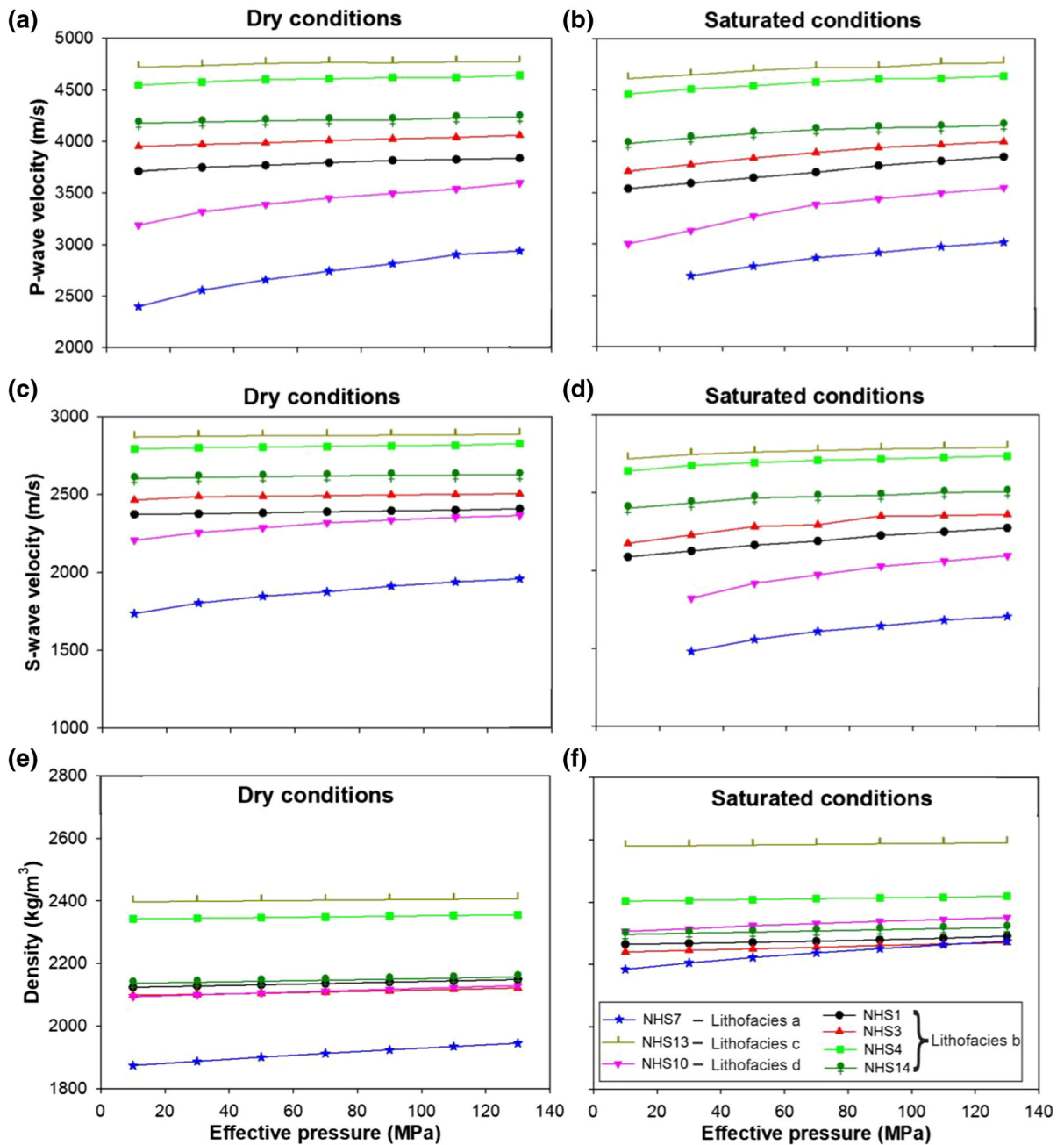


Figure 6

P- (a, b) and S- wave velocities (c, d) and density (e, f) as a function of effective pressure, under dry and saturated conditions

slightly increases. The decrease in the S-wave velocity is greater than the decrease in the P-wave velocity. As the effective pressure increases, the reduction in velocities lessens. The increase in P-wave velocity for the specimen from NHS7 also

lessens with increasing effective pressure. At 10 MPa effective pressure, the P- and S-wave arrival could not be identified for specimen from NHS7 when it was saturated because the waveform was attenuated and within noise, hence the velocities were not

determined. Similarly, the S-wave velocity of the specimen from NHS10 at 10 MPa effective pressure was not determined. The density of the specimens significantly increases when saturated.

The static and dynamic bulk moduli vary for the different lithofacies, with specimens from lithofacies (*c*) and (*a*) having the highest and lowest bulk moduli, respectively (Figs. 7 and 8). Figure 6 shows the static and dynamic bulk moduli with varying effective pressures. We observed that the dynamic Bulk modulus is higher than those of the static in both dry and saturated conditions. For dry and hard lithofacies (specimen from NHS13), the static and dynamic bulk moduli are approximately equal. The bulk modulus increases with increasing effective pressure, which is more dominant for the dynamic bulk modulus. Saturation of the specimens caused the static bulk modulus to decrease and the dynamic bulk modulus to increase. Figure 8 shows $K_{static}/K_{dynamic}$ as a function of effective pressure for dry and saturated specimens. $K_{static}/K_{dynamic}$ ratio of specimens from lithofacies *a* and *d*, shows slight reduction with increasing effective pressure when the specimens are dry. Saturating these specimens, causes a significant decrease in the $K_{static}/K_{dynamic}$ ratio, which increases with increasing effective pressure. Specimens from lithofacies *b* show slight decrease in $K_{static}/K_{dynamic}$ ratio with increasing effective pressure for both dry and saturated conditions. There is no significant change in the $K_{static}/K_{dynamic}$ ratio with increasing effective pressure for the specimen from lithofacies *c*. Under saturated conditions, specimens from lithofacies *b* and *c* also exhibit reduction in $K_{static}/K_{dynamic}$, but not as major as specimens from lithofacies *a* and *d*.

Figure 7 also shows that linear relationships exist between the static and dynamic bulk moduli at varying effective pressures for both dry and saturated conditions. The linear relationships have high correlation of R^2 value equal to 0.85 and greater. In the dry conditions, the gradient and intercept, of the linear relationship, increases and decreases, respectively, with increasing effective pressure (Fig. 9). When saturated, the gradient and intercept follow the same trend as the dry conditions, but the gradient is higher and the intercept is significantly lower.

4. Discussion

In this study, we aimed to sample a minimum of three locations per lithofacies to quantify the heterogeneity, but the terrain, accessibility, and difficulties in retrieving samples limited the study to only a total of seven locations. However, we measured the static and dynamic bulk moduli simultaneously for each outcrop, which removes any heterogenetic effects that could possibly influence the difference between the static and dynamic measurements. Our results show that the dynamic bulk modulus is greater than the static bulk modulus, which is in agreement with previous studies (Adam & Batzle, 2008; Adelinet et al. 2010; Bakhorji & Schmitt, 2010; Batzle et al. 2006; Blake & Faulkner, 2016; Cheng & Johnston, 1981; Jizba & Nur, 1990; Simmons & Brace, 1965). Saturation causes the difference between the static and dynamic elastic properties to increase. This is because it reduces the static bulk modulus and increases the dynamic bulk modulus. Saturation causes the P- and S-wave velocities to decrease, but it also causes the density to increase (Fig. 6) because water fills the pore spaces and creates excess mass, which resulted in an increase in the dynamic bulk modulus. The porosity of the argillites plays an important role in the increase in the dynamic bulk modulus. When the pore spaces are saturated, a new term, the bulk modulus of the pore fluid (K_f), will be added to the bulk modulus of the rock frame (K_{fr}). The results due to saturation are similar to the results by Adelinet et al. (2010) and Blake and Faulkner (2016).

We measured the static and dynamic bulk moduli of soft and hard lithofacies, where the static bulk modulus ranged from 2.2 to 28.7 GPa and dynamic bulk modulus ranged from 3.2 to 31.9 GPa. A high bulk modulus implies that the rock is hard and resists hydrostatic compression. Table 1 shows the porosity and mineralogy composition of the argillites. The soft rocks (lithofacies *a* and *d*) have high porosity and mainly silica content, whereas the hard rocks (lithofacies *b* and *c*) have lower porosity and are dominated by silica and carbonate. The carbonate content in the lithofacies mainly acts to cement the argillites (Iyare et al. 2020), which causes the bulk modulus to be high. The difference between static and dynamic bulk moduli is reduced as the bulk moduli increase. Hence, the stiffer the rock, the closer

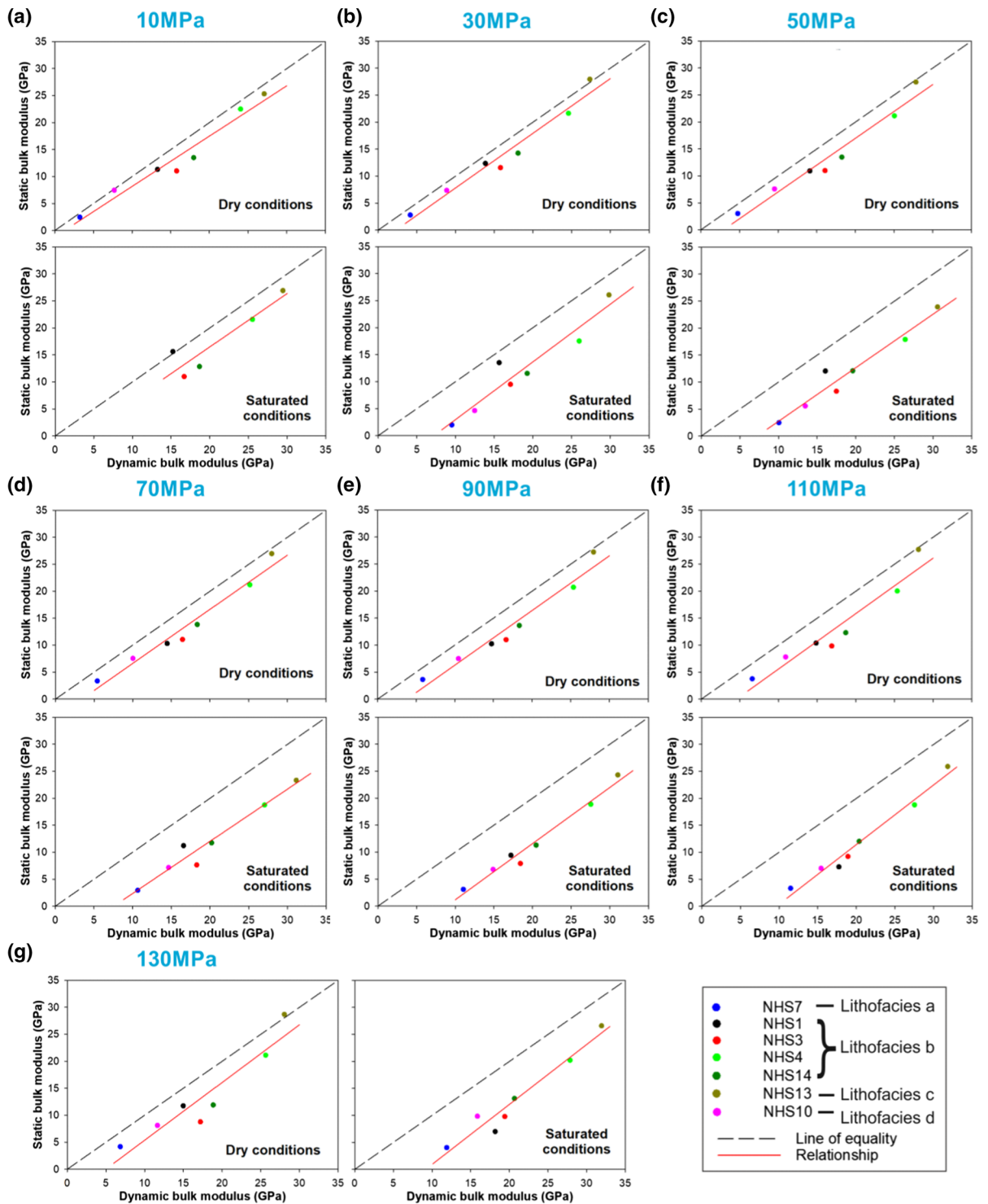


Figure 7

Comparison between static and dynamic bulk moduli at 10, 30, 50, 70, 90, 110 and 130 MPa effective pressure for dry and saturated conditions. Red line represents linear relationship. The static and dynamic error is less than 7 and 1%, respectively

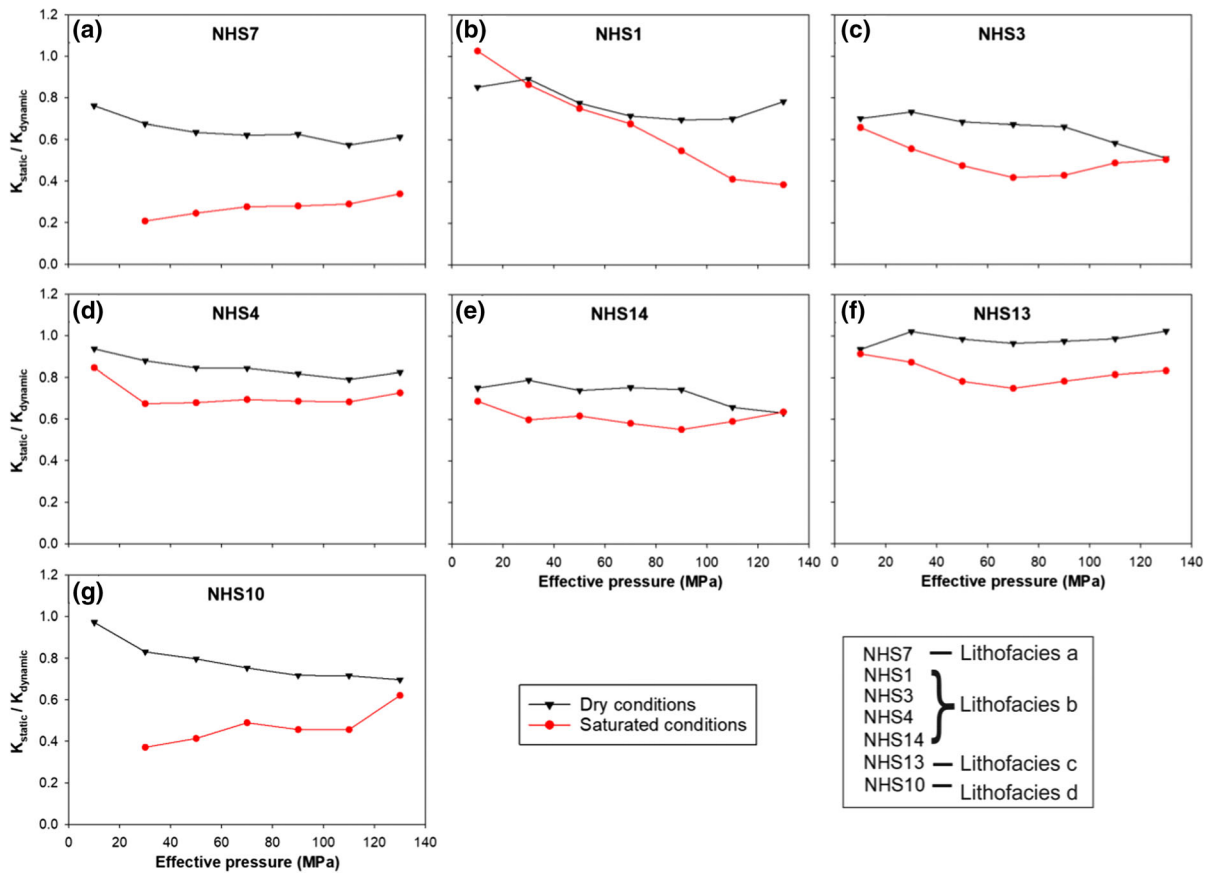


Figure 8

$K_{static}/K_{dynamic}$ ratios as a function of effective pressure under dry and saturated conditions. The static and dynamic error is less than 7 and 1%, respectively

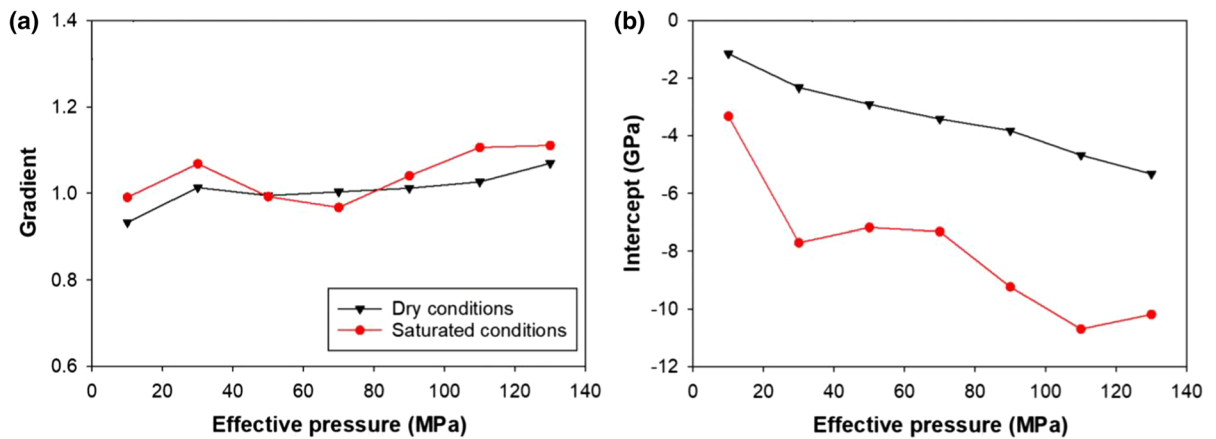


Figure 9

Static and dynamic bulk moduli linear relationship as a function of effective pressure for dry and saturated conditions

Table 1

Porosity (Φ), and mineral compositions of the Naparima Hill outcrop locations (from Iyare et al. (2020))

Lithofacies	Outcrop locations	Φ (%)	Silica Content (Wt. %)	Carbonate Content (Wt. %)	Clay Content (Wt. %)
Lithofacies a	NHS7	30.8 ± 0.2	94	0	6
Lithofacies b	NHS1	14.0 ± 0.7	77	14	7
	NHS3	14.2 ± 0.2	77	12	8
	NHS4	5.9 ± 2.6	62	34	2
	NHS14	16.0 ± 0.2	75	18	6
Lithofacies c	NHS13	18.2 ± 1.2	49	39	2
Lithofacies d	NHS10	20.9 ± 0.6	93	0	7

the static bulk modulus to the dynamic bulk modulus (Wang, 2000). This explains the static and dynamic bulk moduli being approximately equal for the hard lithofacies (lithofacies *c*, specimen from NHS13).

Empirical relationships between the static and dynamic bulk moduli are limited in the literature. We established a linear relationship with high correlation between the static and dynamic bulk moduli of argillites and quantified how this relationship changes as a function of effective pressure (equivalent to burial depth) and saturation state. Jizba and Nur (Jizba & Nur, 1990) also established a linear relationship between the static and dynamic bulk moduli for dry tight gas sandstones, at various confining pressures from 5 to 125 MPa. To get a direct comparison with the study done by Jizba and Nur (Jizba & Nur, 1990), we applied a linear fit ($r^2 = 0.93$) to the present study's entire data (from 10 to 130 MPa effective pressure) for the dry conditions obtaining:

$$K_{static} = 0.996K_{dynamic} - 3.157 \quad (4)$$

This relationship is in agreement with the linear relationship proposed by Jizba and Nur (Jizba & Nur, 1990) (less than 3 GPa difference), within the dynamic range of 19–38 GPa (Fig. 10). As the agreement is for such a small range (dynamic bulk modulus of 19–38 GPa), this suggests that the empirical relationships may be dependent on the rock type.

4.1. Effect of Microfractures and Effective Pressure on the K_{static} and $K_{dynamic}$.

The presence of microfractures affects the stiffness of the rock, reducing the bulk modulus. Microfracture also plays a key role in the difference

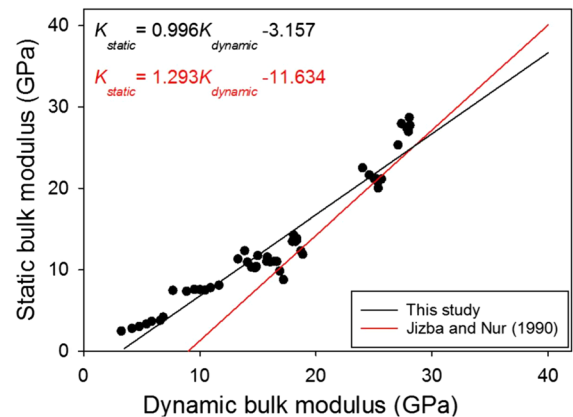


Figure 10

Relationship between the Static and dynamic bulk modulus from the literature and present study. The filled circles represent the present study entire dataset under dry conditions

between the static and dynamic elastic properties. Static elastic bulk modulus is affected by all the fractures, while the dynamic elastic bulk modulus is only affected by fractures that are in the path of the travelling P- and S-waves. If the microfractures are closed then the static and dynamic bulk moduli should be closer to each other (Blake & Faulkner, 2016; Cheng & Johnston, 1981; Simmons & Brace, 1965). Subjecting a rock to effective pressure closes fractures. A plot of velocity vs effective pressure can be used to clearly demonstrate closure of fractures and show the pressure at which all low aspect ratio microfractures are closed. The velocity increases rapidly in a non-linear manner below the fracture-closure pressure, and then increase approximately linearly as effective pressure increases (Birch, 1960; Blake et al. 2013; Kern, 1978). The linear increase may be due to high aspect ratio microfracture, microfractures with mismatched faces and or

compaction of pores. High aspect ratio microfractures and microfractures with mismatched faces require very large effective pressures to close them completely. The velocity vs effective pressure plots seen in Fig. 6 have only linear increase in velocity. This suggests that mainly high aspect ratio microfracture and microfracture with mismatched faces are present in the argillites. This is corroborated with thin section analysis done by (Iyare et al. 2020) (Fig. 2).

Blake and Faulkner (2016) found that the increase of $K_{static}/K_{dynamic}$ ratio with increasing effective pressure is dependent on the fracture density. Westerly granite samples were used in their study, which have low aspect ratio microfractures and microfractures with matched faces. These fracture types are easier to close compared to the microfracture types in the present study. Blake and Faulkner (2016) found that the higher the fracture density, the lower the $K_{static}/K_{dynamic}$ ratio at low effective pressures. The $K_{static}/K_{dynamic}$ ratio converges towards 1 at higher pressure. The rate of increase of the $K_{static}/K_{dynamic}$ ratio is high at low effective pressures, but decreases with increasing effective pressure. This suggests that the closing of microfractures increases the static bulk modulus much more than the dynamic bulk modulus. Figure 8 shows a general trend of $K_{static}/K_{dynamic}$ ratios slightly decreasing with increasing effective pressure. This is most likely due to the low fracture density (Fig. 2) and compaction of the matrix (intrinsic properties), which result in a more dominant increase in the dynamic bulk modulus compared to the static bulk modulus.

4.2. Evaluation of the Anisotropy in the Argillites

The major assumption made in our analysis is isotropy. In general, most natural rocks are anisotropic, because of factors including foliation, oriented fracture networks and mineral preferred orientation. Assuming anisotropic rocks to be isotropic can lead to some degree of discrepancy in the analysis. To evaluate the anisotropy in the argillites, we measured P- and S-wave velocities on orthogonally plugged specimens that were taken from in-situ blocks, from each of the studied locations. Velocities were measured perpendicular (90°) to outcrop bedding, and parallel to outcrop bedding in the strike direction

(0° —S) and dip direction (0° —D) (Table 2). The oil within these specimens were not removed, and the specimens were dried and subjected to effective pressures up to 130 MPa. The anisotropy of the argillites ranged between 2 and 27% (Table 2 and Fig. 11). An increase in the effective pressure caused the anisotropy to reduce, which may be mainly due to fracture closure and compaction of the rock leading to loss of porosity. This is evident as the reduction in the anisotropy is directly proportional to the porosity of the lithofacies. Figure 11 and Table 2 show that lithofacies *a* (31% porosity) has the greatest reduction in the anisotropy, followed by lithofacies *d* (21% porosity), *c* (18% porosity) and *b* (less than 16% porosity). The P- and S-wave anisotropies are less than 10% for the four sample locations within lithofacies *b*. For lithofacies *a*, the P-wave and S-wave anisotropies are 27 and 21%, respectively, at 10 MPa effective pressure and reduced to 17 and 13% at 130 MPa effective pressure. For lithofacies *c* and *d*, the P-wave anisotropy is less than 17%, whereas the S-wave anisotropy is less than 12%. It can be concluded that the results presented in this study have some degree of uncertainty, especially for lithofacies *a*, *c*, and *d* that displayed moderate anisotropy. However, the uncertainty is reduced for results calculated at higher effective pressures as the rocks become more isotropic with increasing effective pressure.

It is better to assume that these argillites are transversely isotropic with the plane of transverse isotropy in the direction parallel to the bedding of the outcrop. This is because the P- and S-wave velocities are approximately equal in the strike and dip directions of the beds (Table 2). For a transversely isotropic rock, five independent materials parameters need to be determined which involves measuring: (1) the Young's modulus in the direction parallel and perpendicular to the plane of transverse isotropy (outcrop bedding); (2) Poisson's ratio in the direction parallel and perpendicular to the plane of transverse isotropy; and (3) shear modulus in the direction perpendicular to the plane of transverse isotropy. When a rock is isotropic, only two independent elastic constants are required to fully characterize the elasticity of the rock (for example, Young's modulus and Poisson's ratio), from which the other elastic

Table 2

P- and S-wave velocities anisotropies in the argillites (modified from Blake et al. (2020))

Lithofacies	Sample location	P _{eff} (MPa)	VP (90°) (m/s)	VP (0° - S) (m/s)	VP (0° - D) (m/s)	VS (90°) (m/s)	VS (0° - S) (m/s)	VS (0° - D) (m/s)	V _p anisotropy (%)	V _s anisotropy (%)
Lithofacies a	NHS7	10	2200	2912	2859	1537	1877	1533	26.8	20.8
		30	2382	3038	2984	1628	1878	1597	23.4	16.5
		50	2494	3121	3171	1679	1913	1647	21.4	15.2
		70	2624	3187	3180	1728	1932	1678	18.8	14.3
		90	2705	3289	3198	1772	1953	1722	19.0	12.7
		110	2749	3300	3212	1789	1983	1740	17.9	13.2
Lithofacies b	NHS1	130	2806	3327	3254	1816	1997	1761	16.6	12.7
		10	3627	3925	3910	2301	2428	2259	7.8	7.2
		30	3679	3962	3939	2311	2432	2284	7.4	6.3
		50	3716	3991	3965	2317	2434	2287	7.1	6.3
		70	3750	4010	3981	2325	2444	2335	6.6	4.6
		90	3766	4030	3994	2331	2455	2340	6.7	4.8
	NHS3	110	3792	4046	4014	2356	2461	2346	6.4	4.8
		130	3818	4070	4044	2359	2467	2354	6.3	4.7
		10	3797	3807	3884	2325	2292	2399	2.3	4.6
		30	3820	3844	3939	2344	2308	2416	3.1	4.6
		50	3839	3875	3974	2363	2321	2423	3.5	4.3
		70	3869	3891	3999	2373	2329	2470	3.3	5.9
	NHS4	90	3900	3913	4003	2392	2338	2471	2.6	5.6
		110	3914	3936	4013	2394	2345	2473	2.5	5.3
		130	3931	3949	4039	2405	2348	2479	2.7	5.4
		10	4023	4494	4381	2563	2713	2702	10.9	5.6
		30	4095	4507	4442	2595	2738	2711	9.5	5.3
		50	4110	4512	4446	2606	2751	2713	9.2	5.4
	NHS14	70	4144	4557	4465	2610	2777	2725	9.4	6.2
		90	4159	4562	4508	2612	2789	2736	9.1	6.5
		110	4178	4567	4513	2613	2791	2738	8.8	6.5
		130	4189	4571	4527	2616	2806	2745	8.6	7.0
		10	3939	4036	3935	2502	2439	2494	2.5	2.5
		30	4003	4092	3964	2514	2450	2511	3.2	2.6
Lithofacies c	NHS13	50	4017	4109	3971	2523	2464	2520	3.4	2.4
		70	4031	4127	3985	2527	2474	2523	3.5	2.1
		90	4048	4150	4011	2534	2475	2526	3.4	2.3
		110	4059	4159	4018	2545	2482	2531	3.4	2.5
		130	4080	4163	4040	2552	2485	2534	3.0	2.7
		10	3735	4361	4436	2458	2714	2594	16.8	9.9
	NHS10	30	3818	4410	4455	2477	2726	2604	15.1	9.6
		50	3874	4455	4504	2497	2733	2619	14.7	9.0
		70	3920	4474	4514	2511	2740	2626	13.8	8.7
		90	3960	4488	4549	2529	2745	2636	13.6	8.2
Lithofacies d	NHS10	110	3992	4506	4554	2550	2750	2639	12.9	7.6
		130	4037	4516	4564	2573	2755	2646	12.1	6.8
		10	2903	3500	3487	1976	2046	2290	18.1	11.6
		30	3042	3609	3619	2037	2113	2304	16.9	8.9
		50	3097	3650	3683	2073	2153	2316	16.8	7.5
		70	3214	3712	3720	2098	2176	2327	14.3	6.8
		90	3247	3745	3787	2123	2196	2347	15.0	6.8
		110	3270	3752	3819	2145	2221	2361	15.2	6.2
		130	3325	3786	3826	2153	2227	2371	13.8	6.4

V_p and V_s measurements were made on plug samples that were taken perpendicular (90°) to bedding, strike direction (0°—S), and dip direction (0°—D). Strike and dip directions are parallel to bedding and perpendicular to each other. Velocity measurements were made at 10, 30, 50, 90, 110 and 130 MPa effective pressure (P_{eff}) under dry conditions. The anisotropy % is calculated by: ((maximum velocity—minimum velocity) / mean velocity) × 100

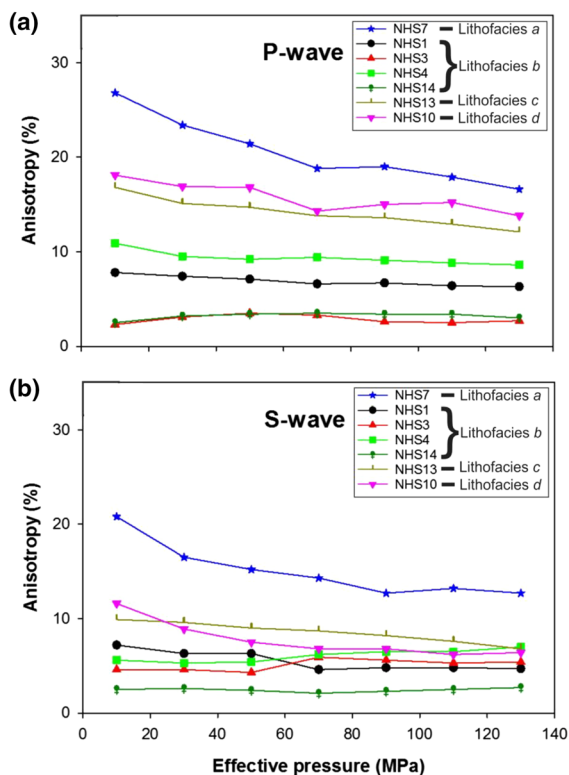


Figure 11

P-wave (a) and S-wave (b) anisotropies as a function of effective pressure in the argillites (modified from Blake et al. (2020))

constants can be easily calculated (for example, bulk modulus, shear modulus and Lamé's first parameter). Completely characterizing the static and dynamic elastic anisotropies of these argillites requires simultaneous static (stress–strain) and dynamic measurements (P- and S-wave velocities) on specimens that are plugged perpendicular, parallel, and 45° to the outcrop bedding (e.g. Amadei, 1996; Dewhurst & Siggins, 2006; Homand et al. 1993; Lo et al. 1986; Sone & Zoback, 2013). Sone and Zoback (2013) evaluated the error of assuming that a rock is isotropic rather than transversely isotropic for 16 different anisotropic shale samples and reported that the error in the Young's modulus is within 5%. This suggests that the degree of uncertainty in our results, due to the assumption that the argillites are isotropic, is small, especially for argillites with low anisotropy.

5. Summary

The static and dynamic bulk moduli were measured simultaneously, at effective pressure up to 130 MPa, for dry and fluid-saturated organic-rich argillite specimens. We found that the dynamic bulk modulus is greater than the static bulk modulus. For dry and harder rocks (bulk modulus of approximately 28 GPa) both moduli are roughly equal. Saturation of the specimens increases the difference between the static and dynamic bulk moduli, which proves to be significant for weaker lithofacies.

Relationships that relate static to dynamic bulk modulus of argillites do not exist in the literature. We established a linear relationship between the static and dynamic bulk moduli and found that the relationship is dependent on the effective pressure (equivalent to burial depth) and saturation state. The few empirical relationships that exist in the literature are not in total agreement, which suggests that the relationships are dependent on the rock type. Hence, core or outcrop measurements for both the dynamic and static bulk moduli should be carried out to establish type locality and regional empirical relationships for the interested fields or reservoirs.

Acknowledgements

We would like to thank the Ministry of Energy and Energy Industries, Trinidad and Tobago, Engineering Institute, Faculty of Engineering, and Campus Research and Publication Fund Committee, University of the West Indies, St. Augustine Campus, for funding of this research.

Funding

The authors have no relevant financial or non-financial interests to disclose.

Compliance with ethical standards

Conflicts of interest The authors have no conflicts of interest to declare.

Publisher's Note Springer Nature remains neutral with regard to jurisdictional claims in published maps and institutional affiliations.

REFERENCES

- Adam, L., & Batzle, M. (2008). Elastic properties of carbonates from laboratory measurements at seismic and ultrasonic frequencies. *The Leading Edge*, 27(8), 1026–1032. <https://doi.org/10.1190/1.2967556>
- Adelinet, M., Fortin, J., Guéguen, Y., Schubnel, A., & Geoffroy, L. (2010). Frequency and fluid effects on elastic properties of basalt: experimental investigations. *Geophysical Research Letters*, 37(2), L02303. <https://doi.org/10.1029/2009gl041660>
- Amadei, B. (1996). Importance of anisotropy when estimating and measuring in situ stresses in rock. *International Journal of Rock Mechanics and Mining Sciences & Geomechanics Abstracts*, 33(3), 293–325. [https://doi.org/10.1016/0148-9062\(95\)00062-3](https://doi.org/10.1016/0148-9062(95)00062-3)
- ASTM-D2845 (2008). Standard test method for laboratory determination of pulse velocities and ultrasonic elastic constants of rock Vol. 4.08. West Conshohocken, PA: ASTM International.
- ASTM-D4543. (2019). *Standard practices for preparing rock core as cylindrical test specimens and verifying conformance to dimensional and shape tolerances: annual book of astm standards*. American Society for Testing and Materials.
- ASTM-D7012 (2014). Standard test method for compressive strength and elastic moduli of intact rock core specimens under varying states of stress and temperatures Vol. 4.08. West Conshohocken, PA: ASTM International.
- Bakhorji, A., & Schmitt, D. R. (2010). *Laboratory measurements of static and dynamic bulk moduli in carbonate*. In Paper presented at the 44th U.S. Rock Mechanics Symposium and 5th U.S.-Canada Rock Mechanics Symposium, Salt Lake City, Utah, 2010/1/1/.
- Batzle, M., Han, D. H., & Hofmann, R. (2006). Fluid mobility and frequency-dependent seismic velocity-direct measurements. *Geophysics*, 71(1), N1–N9.
- Batzle, M., Hofmann, R., Han, D.-H., & Castagna, J. (2001). Fluids and frequency dependent seismic velocity of rocks. *The Leading Edge*, 20(2), 168–171. <https://doi.org/10.1190/1.1438900>
- Birch, F. (1960). The velocity of compressional waves in rocks to 10-kilobars. 1. *Journal of Geophysical Research*, 65(4), 1083–1102.
- Blake, O. O., & Faulkner, D. R. (2016). The effect of fracture density and stress state on the static and dynamic bulk moduli of Westerly granite. *Journal of Geophysical Research: Solid Earth*, 121(4), 2382–2399. <https://doi.org/10.1002/2015JB012310>
- Blake, O. O., Faulkner, D. R., & Rietbrock, A. (2013). The effect of varying damage history in crystalline rocks on the P- and S-wave velocity under hydrostatic confining pressure. *Pure and Applied Geophysics*, 170(4), 493–505. <https://doi.org/10.1007/s00024-012-0550-0>
- Blake, O. O., Ramsook, R., Faulkner, D. R., & Iyare, U. C. (2020). The effect of effective pressure on the relationship between static and dynamic young's moduli and poisson's ratio of naparima hill formation mudstones. *Rock Mechanics and Rock Engineering*. <https://doi.org/10.1007/s00603-020-02140-0>
- Cheng, C. H., & Johnston, D. H. (1981). Dynamic and static moduli. *Geophysical Research Letters*, 8(1), 39–42. <https://doi.org/10.1029/GL008i001p00039>
- Dewhurst, D. N., & Siggins, A. F. (2006). Impact of fabric, microcracks and stress field on shale anisotropy. *Geophysical Journal International*, 165(1), 135–148. <https://doi.org/10.1111/j.1365-246X.2006.02834.x>
- Gupta, I., Rai, C., Tinni, A., & Sondergeld, C. (2017). Impact of different cleaning methods on petrophysical measurements. *Petrophysics*, 58(06), 613–621.
- Hammond, J. P., Ratcliff, L. T., Brinkman, C. R., & Nestor, J. C. W. (1979). *Dynamic and static measurements of elastic constants with data on 2 1/4 Cr-1 mo steel, types 304 and 316 stainless steels, and alloy 800H* (ORNL-5442, Vol. ORNL-5442). Oak Ridge, TN: ORNL-5442, Oak Ridge National Laboratory.
- Homand, F., Morel, E., Henry, J.-P., Cuxac, P., & Hammade, E. Characterization of the moduli of elasticity of an anisotropic rock using dynamic and static methods. In *International journal of rock mechanics & mining sciences & geomechanics abstracts*, 1993 (Vol. 30, pp. 527–535, Vol. 5): Elsevier.
- Iyare, U. C., Ramsook, R., Blake, O. O., & Faulkner, D. R. (2020). Petrographical and petrophysical characterization of the late cretaceous Naparima Hill Formation, Central Range, Trinidad, West Indies. *International Journal of Coal Geology*, 230, 103592. <https://doi.org/10.1016/j.coal.2020.103592>
- Jizba, D. (1991). *Mechanical and acoustical properties of sandstones and shales*. Stanford University.
- Jizba, D., & Nur, A. (1990). *Static And Dynamic Moduli Of Tight Gas Sandstones And Their Relation To Formation Properties*. In Paper presented at the SPWLA 31st Annual Logging Symposium, Lafayette, Louisiana, 1990/1/1/.
- Kern, H. (1978). The effect of high temperature and high confining pressure on compressional wave velocities in quartz-bearing and quartz-free igneous and metamorphic rocks. *Tectonophysics*, 44(1–4), 185–203. [https://doi.org/10.1016/0040-1951\(78\)90070-7](https://doi.org/10.1016/0040-1951(78)90070-7)
- Lo, T.-W., Coyner, K. B., & Toksöz, M. N. (1986). Experimental determination of elastic anisotropy of Berea sandstone, Chicopee shale, and Chelmsford granite. *Geophysics*, 51(1), 164–171.
- Müller, T. M., Gurevich, B., & Lebedev, M. (2010). Seismic wave attenuation and dispersion resulting from wave-induced flow in porous rocks—a review. *Geophysics*, 75(5), 175A147–175A164.
- Pindell, J. L., & Kennan, L. (2009). Tectonic evolution of the Gulf of Mexico, Caribbean and northern South America in the mantle reference frame: an update. *Geological Society, London, Special Publications*, 328(1), 1–55. <https://doi.org/10.1144/sp328.1>
- Simmons, G., & Brace, W. F. (1965). Comparison of static and dynamic measurements of compressibility of rocks. *Journal of Geophysical Research*, 70(22), 5649–5656. <https://doi.org/10.1029/JZ070i022p05649>
- Sone, H., & Zoback, M. D. (2013). Mechanical properties of shale-gas reservoir rocks—Part I: Static and dynamic elastic properties and anisotropy. *Geophysics*, 78(5), D381–D392. <https://doi.org/10.1190/geo2013-0050.1>
- Tutuncu, A. N., Podio, A. L., Gregory, A. R., & Sharma, M. M. (1998a). Nonlinear viscoelastic behavior of sedimentary rocks, Part I: Effect of frequency and strain amplitude. *Geophysics*, 63(1), 184–194.
- Tutuncu, A. N., Podio, A. L., & Sharma, M. M. (1998b). Nonlinear viscoelastic behavior of sedimentary rocks, Part II: Hysteresis

- effects and influence of type of fluid on elastic moduli. *Geophysics*, 63(1), 195–203.
- Wang, Z. (2000). Dynamic versus static elastic properties of reservoir rocks. *Society of Exploration Geophysicists*, 3, 531–539.
- Yan, F., Han, D.-H., Ren, J., Wang, Y., & Chen, X.-L. (2017). *Comparison of dynamic and static bulk moduli of reservoir rocks*. Paper presented at the 2017 SEG International Exposition and Annual Meeting, Houston, Texas, 2017/10/23/

(Received April 28, 2020, revised February 17, 2021, accepted February 19, 2021, Published online March 3, 2021)